ADVANCED MATERIALS INTERFACES
Open Access

Precision Calcination Mechanism of $CaCO_3$ to High-Porosity Nanoscale CaO CO_2 Sorbent Revealed by Direct In Situ Observations

*Jenny Martinez, Jenna L. Wardini, Xueli Zheng, Lauren Moghimi, Jason Rakowsky, Jonathan Means, Huiming Guo, Ivan Kuzmenko, Jan Ilavsky, Fan Zhang, Pratik P. Dholabhai, Leora Dresselhaus-Marais, and William J. Bowman****

Deploying energy storage and carbon capture at scale is hindered by the substantial endothermic penalty of decomposing $CaCO_3$ to CaO and CO_2, and the rapid loss of CO_2 absorption capacity by CaO sorbent particles due to sintering at the high requisite decomposition temperatures. The decomposition reaction mechanism underlying sorbent deactivation remains unclear at the atomic level and nanoscale due to past reliance on postmortem characterization methods with insufficient spatial and temporal resolution. Thus, elucidating the important $CaCO_3$ decomposition reaction pathway requires direct observation by time-resolved (sub-)nanoscale methods. Here, chemical and structural dynamics during the decomposition of $CaCO_3$ nanoparticles to nanoporous CaO particles comprising high-surface-area CaO nanocrystallites are examined. Comparing in situ transmission electron microscopy (TEM) and synchrotron X-ray diffraction experiments gives key insights into the dynamics of nanoparticle calcination, involving anisotropic $CaCO_3$ thermal distortion before conversion to thermally dilated energetically stable CaO crystallites. Time-resolved TEM uncovered a novel CaO formation mechanism involving heterogeneous nucleation at extended $CaCO_3$ defects followed by sweeping reaction front motion across the initial $CaCO_3$ particle. These observations clarify longstanding, yet incomplete, reaction mechanisms and kinetic models lacking accurate information about (sub-)nanoscale dynamics, while also demonstrating calcination of $CaCO_3$ without sintering through rapid heating and precise temperature control.

1. Introduction

The reactions between solid CaO and CO_2 gas are fundamental in geology,[1–3] energy storage,[4,5] CO_2 capture and utilization,[6–9] animal-machine interface,[10] chemical synthesis from CO_2,[11,12] cement production,[13–15] space exploration,[16] and maritime mobility.[17] Despite its importance, the highly endothermic ($\Delta H^0_{298\ K} = 178$ kJ mol^{-1}) $CaCO_3$ calcination reaction mechanism remains misunderstood due to a lack of direct (sub-)nanoscale observation. $CaCO_3$ calcination is a model solid-vapor decomposition reaction and is the critical step in calcium looping ($CaCO_{3(s)}$ + Energy ↔ $CaO_{(s)}$ + $CO_{2(g)}$). This cycle offers among the highest experimentally demonstrated (0.75 $gCO_2/gCaO$)[18] and theoretical (0.786 $gCO_2/gCaO$)[19] CO_2 uptake capacity to date, and high thermochemical energy storage density (3.26 GJ m^{-3}).[20,21] However, after decades of research, the underlying calcination mechanism remains unclear and/or controversial[22–24] with respect

---

J. Martinez, J. L. Wardini, J. Means, H. Guo, W. J. Bowman
Department of Materials Science and Engineering
University of California Irvine
Irvine, CA 92697, USA
E-mail: will.bowman@uci.edu

X. Zheng, L. Moghimi, L. Dresselhaus-Marais
Department of Materials Science and Engineering
Stanford University
Stanford, CA 94305, USA

The ORCID identification number(s) for the author(s) of this article can be found under https://doi.org/10.1002/admi.202300811

DOI: 10.1002/admi.202300811

X. Zheng, L. Moghimi, L. Dresselhaus-Marais
SLAC National Accelerator Laboratory
Menlo Park, CA 94025, USA

J. Rakowsky, P. P. Dholabhai
School of Physics and Astronomy
Rochester Institute of Technology
New York, NY 14623, USA

I. Kuzmenko, J. Ilavsky
X-ray Science Division
Argonne National Laboratory
Lemont, IL 60439, USA

F. Zhang
Materials Measurement Science Division
National Institute of Standards and Technology
Gaithersburg, MD 20899, USA

to the crystal structures and the evolution of multiscale morphologies under different kinetic regimes,[25,26] leading to inconsistent data interpretation.

Unfortunately, large-scale deployment of Ca-looping technologies is limited by the rapid deactivation of CaO as a CO_2 sorbent after only tens to hundreds of cycles. This has been attributed to CaO particle coarsening, sintering, surface area loss,[27,28] and product layer growth,[29] during calcination[30] though these mechanistic details remain unclear. At the single-particle level, the $CaCO_3$ calcination mechanism is widely described using a shrinking core model,[31,32] although complex multiscale (> 100 nm) pore structures/networks have been observed in large (mm-scale) particles.[33] Some argue that sintering occurs when particles are $CaCO_3$, because typical calcination temperatures (≈900 °C) exceed the $CaCO_3$ sintering onset ("Tammann") temperature of 533 °C.[34] Others claim that sintering occurs after CaO formation—even though the CaO Tammann temperature (1170–1313 °C[6,35]) exceeds typical calcination temperatures—because a metastable dilated CaO intermediate phase sinters due to exothermic relaxation to the thermodynamically stable unstrained CaO. However, the existence and role of a metastable CaO intermediate remains controversial after ≈50 years,[36–41] with researchers still debating if it is a key short-lived reaction intermediate responsible for sorbent surface area loss before transformation to stable CaO. It is currently not clear how the morphology of the solid and its evolution during thermal decomposition affects the conceptual picture describing the reaction progress/dynamics; we use the term "reaction mechanism" here to describe this.[26] Consequently, there is disagreement on the rate equation constants and associated calcination models used to interpret reaction rates which have been shown to vary by several orders of magnitude between publications.[42] A major challenge to clarifying the mechanism has been a heavy reliance on analytical methods that do not directly observe atomic and surface structure-reactivity relationships in situ, such as thermogravimetric and postmortem structure chemical analyses, resulting in a lack of consensus on the calcination mechanism and rate-limiting steps.[22,26,43]

Here, in situ transmission electron microscopy (TEM) and synchrotron X-ray diffraction (XRD) reveal a nanoscale $CaCO_3$ calcination reaction model involving heterogeneous nucleation of nanoporous CaO at $CaCO_3$ grain boundaries followed by planar reaction front motion, in contrast to the widely accepted spherical shrinking core model. The benefits of such advanced characterization techniques include their ability to directly investigate structural, chemical, and morphological features, fundamental atomic-scale disorder, chemical reactions, and/or interphase formation.[44,45] We examine chemical and structural dynamics during the thermal decomposition of <100 nm $CaCO_3$ particles to nanoporous CaO particles with randomly spatially oriented crystallites, providing a milestone in the basic understanding of key physicochemical processes that shorten the service life of CaO (and metal oxide) sorbents and define their CO_2 reactivity and capacity via structure and morphology.[6] We show that calcination involves the anisotropic thermal expansion of calcite (R-3c, hexagonal $CaCO_3$), followed by complete CaO crystallite formation after 2 s at 600 °C yielding intraparticle nanoporosity and high surface area. Regarding the role of the controversial metastable dilated CaO reaction intermediate, we find no evidence for this phase and instead observe nucleation of unstrained CaO whose measured lattice constant matches that of thermodynamically stable CaO predicted by density functional theory (DFT). Importantly for applications, nanoporous CaO particles form at distinctly lower temperatures than particle sintering and surface area loss, demonstrating that sorbent capacity degradation could be avoided. Moreover, the calcined CaO morphology offers a high surface-area-to-volume ratio, expected to provide higher reactivity[46] and CO_2 uptake rates[47] at lower, more energy-efficient carbonation temperatures than larger sorbent particles.

2. Results

Stepwise in situ TEM heating under vacuum was used to monitor the crystal structure and morphology of 70 nm calcite $CaCO_3$ (hexagonal R-3c) nanoparticles during calcination (**Figure 1**a; Figure S1, Supporting Information). Selected area electron diffraction (SAED) patterns recorded (at room temperature) periodically throughout calcination confirmed that $CaCO_3$ fully transformed to CaO after heating to 600 °C (Figure 1b,c). After heating, continuous SAED rings superimposed with faint spots replaced discrete SAED spots from the polycrystalline $CaCO_3$, indicating the formation of randomly oriented nanocrystalline CaO. The $CaCO_3$ calcination onset and CaO nucleation were observed by azimuthal radially integrated SAED after heating at 500 °C for 20 s, resulting in the coexistence of $CaCO_3$ and CaO evident by the intensification of $CaCO_3$ (006), (110), and (113) peaks due to contribution from emerging broad CaO (111) and (200) peaks (Figure 1d; Figure S2 and Table S1, Supporting Information). Heating to 600 °C for 20 s yielded complete calcination and exact agreement between SAED and the CaO reference. Further heating to 900 °C produced discrete SAED spots within the continuous CaO diffraction rings, evidence of CaO nanocrystal growth attributed to approaching the CaO sintering onset temperature (Figure S3, Supporting Information).[6,35]

To address the debate about whether an intermediate metastable phase comprising ≈5 nm CaO crystallites forms between calcite and stable CaO during calcination,[48] in situ synchrotron XRD was used to detect reaction intermediates using a more precise diffraction method with greater sampling volume than TEM SAED. $CaCO_3$ consumption and CaO formation were monitored during calcination of 90 nm $CaCO_3$ under 1 atm N_2 until the CaO volume fraction was 10–15%. The higher resolution of synchrotron XRD for d-spacing measurements revealed subtle peak shifts, which were used to quantify the lattice parameters (**Figure 2**; Figures S4–S7 and Table S2, Supporting Information). During in situ XRD the calcination onset temperature was 600 °C (instead of 500 °C during in situ TEM), attributed to higher ambient pressure surrounding the particles and tighter particle packing. This packing density is expected to increase the residence time of CO_2 in the vicinity of the calcining particles, effectively increasing the CO_2 partial pressure and shifting the reaction equilibrium toward the reactants. Anisotropic thermal expansion/contraction of $CaCO_3$ was observed before calcination onset (at 40 and 500 °C): The $CaCO_3$ (116) and (006) peaks shift right (expansion), while the (018), (202), and (110) peaks shift left (contraction).[49] The $CaCO_3$ lattice parameters measured using

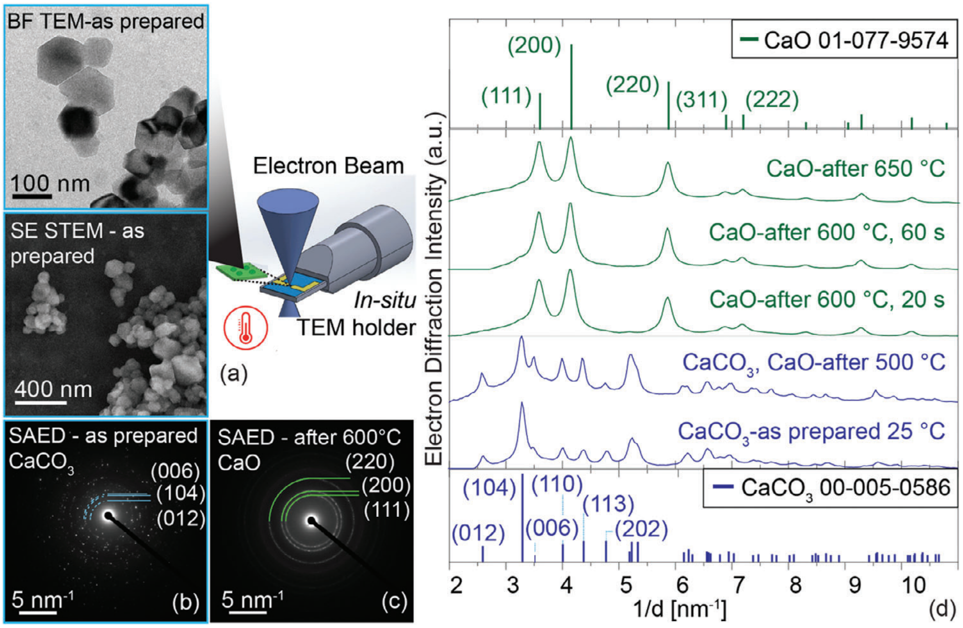

Figure 1. In situ, TEM imaging and selected area electron diffraction (SAED) monitored the calcination of $CaCO_3$ nanoparticles under vacuum. a) BFTEM and STEM secondary electron (SE) images of as-prepared $CaCO_3$ nanoparticles. b,c) TEM SAED patterns were recorded at 25 °C of (b) as-prepared calcite and (c) after transformation to nanocrystalline CaO at 600 °C. d) Azimuthal radial integrations of SAED patterns from as-prepared calcite $CaCO_3$ and calcined CaO agree with JCPDS cards 00-005-0586 and 01-077-9574.

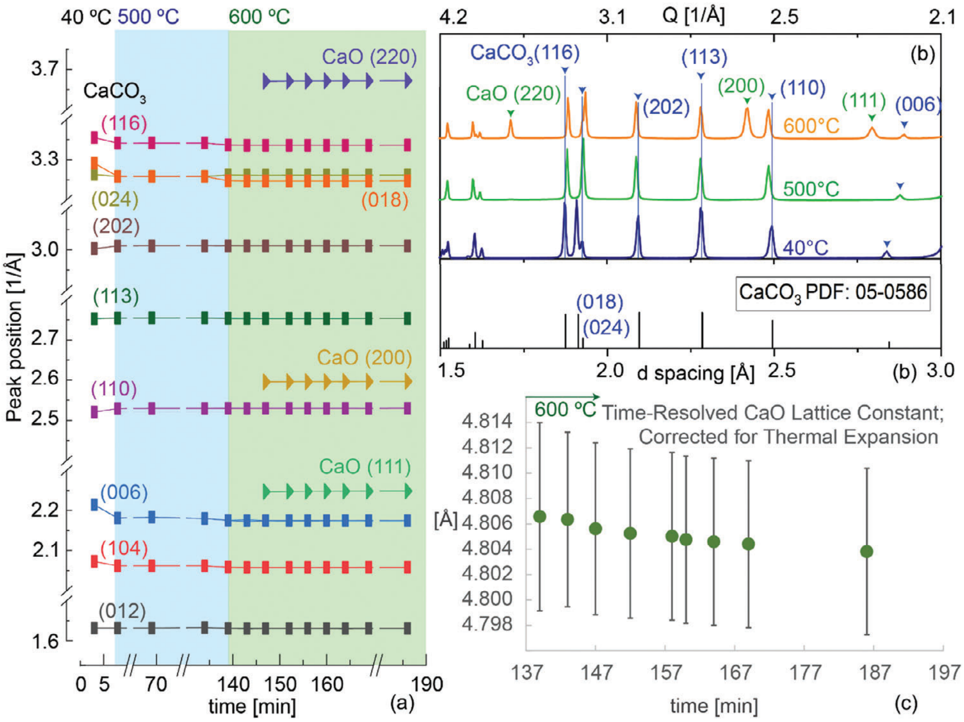

Figure 2. a) Fitting time-resolved in situ synchrotron X-ray diffraction (XRD) patterns to Voigt peaks revealed anisotropic thermal expansion/contraction and that calcination yields stable CaO, evident by static CaO peak positions after calcination onset at 147 min. Under one atm N_2 in a packed bed reactor, the calcination onset shifts to a higher temperature compared to in situ TEM vacuum calcination. b) Select XRD patterns recorded at 40, 500, and 600 °C, showing calcination onset preceded by $CaCO_3$ anisotropic thermal expansion/contraction. The $CaCO_3$ (116), (018), and (006) peaks shift right, while the (202) and (110) peaks shift left and other peaks are static, e.g., (113). CaO peaks labels include "CaO", and color codes apply to (a). c) Fitting the CaO peaks to a Voigt function and calculating the corresponding lattice constants from the peak centroid position. Uncertainty bars indicate the estimated precision of the measured peak position of ± 1 channel in the synchrotron XRD pattern. These data confirm that the CaO lattice parameter is static for the duration of the heating experiment. The first CaO pattern was recorded 5 min after heating to the calcination onset temperature of 600 °C.

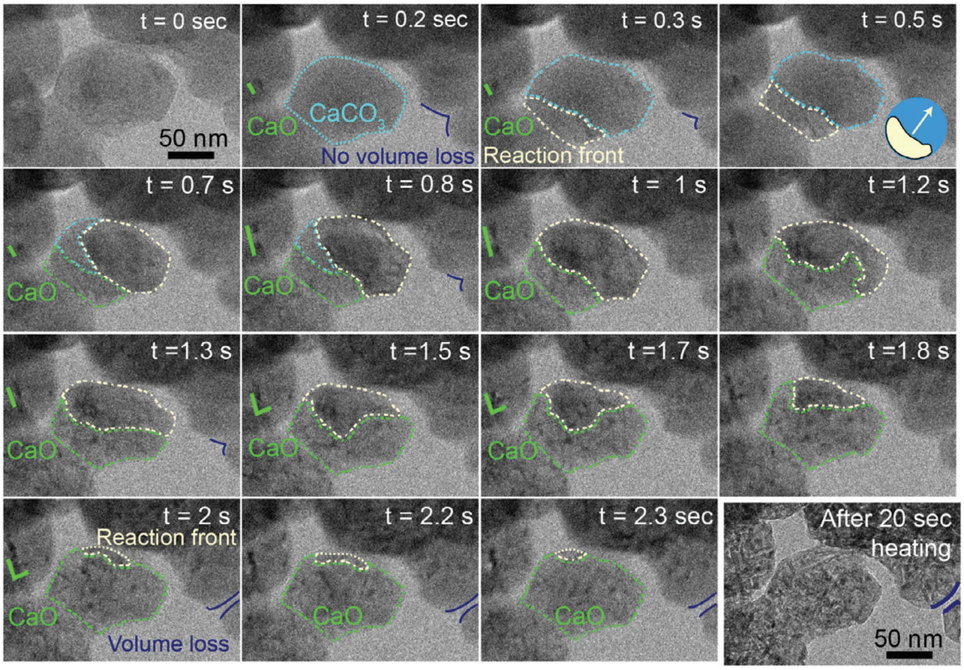

Figure 3. CaCO$_3$ calcination to CaO during in situ TEM heating at 600 °C in vacuum shows CaO crystallite nucleation and growth, reaction front motion, particle size stability, and particle agglomerate volume loss. At 0.2 s of heating, the first isolated CaO crystallite nucleates at a grain boundary (green rectangle). From 0.3–0.5 s, the calcination reaction front (outlined yellow) nucleates at a grain boundary of the central CaCO$_3$ particle (outlined blue) and moves rightward. At 0.7 s, the reaction front moves to the right of the particle, consuming unreacted CaCO$_3$ and leaving behind visible CaO crystallites separated by intraparticle nanoporosity in the converted volume (outlined green). From 0.8–1.0 s, the reaction front consumes all remaining CaCO$_3$ and the converted CaO volume expands rightward. From 1.2–2.3 s, the reaction front propagates counterclockwise, converting the entire particle to nanoporous CaO. After 20 s, the entire sample is nanoporous CaO particles retaining the shape and size of the initial CaCO$_3$ after full calcination.

the position of peaks (006) and (110) at 500 °C are a = b = 4.98 Å ± 0.010 Å and c = 17.03 Å ± 0.04 Å, agreeing well with the reference value of a = b = 4.989 Å and c = 17.06 Å (PDF 05–0586). These values were corrected for the anisotropic thermal expansion of calcite at 500 °C.[49] During calcination (at 600 °C), emergent CaO peak positions were static with time as the CaO volume fraction increased (Figure 2a-c; Figures S5 and S6, Supporting Information). The delayed emergence of CaO peaks at 600 °C by <≈ 5 min indicates their initial diffraction intensity is below the detection limit due to low phase volume and small crystallite size. The CaO lattice constant measured at 600 °C was 4.841 Å ± 0.007 Å (Table S2, Supporting Information). After accounting for CaO[50] thermal expansion (13×10^{-6} K^{-1}) the lattice constant at 25 °C was estimated as 4.805 Å ± 0.007 Å (Figure 2c), agreeing well with the reference value of 4.8107 Å (PDF 01-077-9574). The discrepancy between the XRD-derived lattice constant and reference represents a 0.005 Å contraction of CaO, or <5 meV deviation from the DFT-calculated lowest-energy form of CaO determined by calculating the CaO unit cell energy as a function of lattice expansion (Figure S7, Supporting Information). This supports our interpretation that CaO detected at the onset of calcination is not a strained metastable form that is often cited as the cause of sintering and sorbent deactivation. Summarizing the XRD and DFT results, before calcination CaCO$_3$ undergoes anisotropic expansion/contraction, then during calcination, it converts directly to thermodynamically stable CaO nanocrystallites with lattice dilation accounted for by thermal expansion.

To reveal the local structure-reactivity relationship during calcination and detail the nanoscale reaction model, time-resolved in situ TEM bright field (BF) imaging directly visualized the phase transformation, which followed an unreported reaction pathway. CaCO$_3$ calcination occurred in <2.5 s (**Figure 3**; Movie S1, Supporting Information) and did not follow the currently accepted shrinking core model,[31,32] which predicts that the reaction interface nucleates at the free surfaces and migrates radially inward toward the unreacted CaCO$_3$ particle core. Instead, a planar reaction front nucleated at a CaCO$_3$ grain boundary (i.e., a particle-particle interface) propagated across, around, and through the particle parallel to its surface until all CaCO$_3$ converted to CaO. At 0.2 s, dark diffraction contrast reveals the first CaO nanocrystal forming at a grain boundary (indicated by a parallel adjacent green rectangle labeled 'CaO'), evidence of the relatively lower activation energy required to heterogeneously nucleate calcination at the particle-particle grain boundary compared to the particle interior.[51] Additional postmortem TEM imaging of the onset of calcination indicated the preference for CaO nucleation at CaCO$_3$ grain boundaries (Figure S8, Supporting Information). At 0.3 s (Figure 3), a grain boundary in the central CaCO$_3$ particle (outlined blue) facilitates the initiation of a reaction front (outlined yellow), which exhibits dynamic contrast changes while propagating from left to right. At 0.7 s, the reaction front moves to the right of the particle, consuming unreacted CaCO$_3$ and leaving behind visible CaO crystallites separated by intraparticle nanoporosity in the converted volume (outlined green). At 0.8 s,

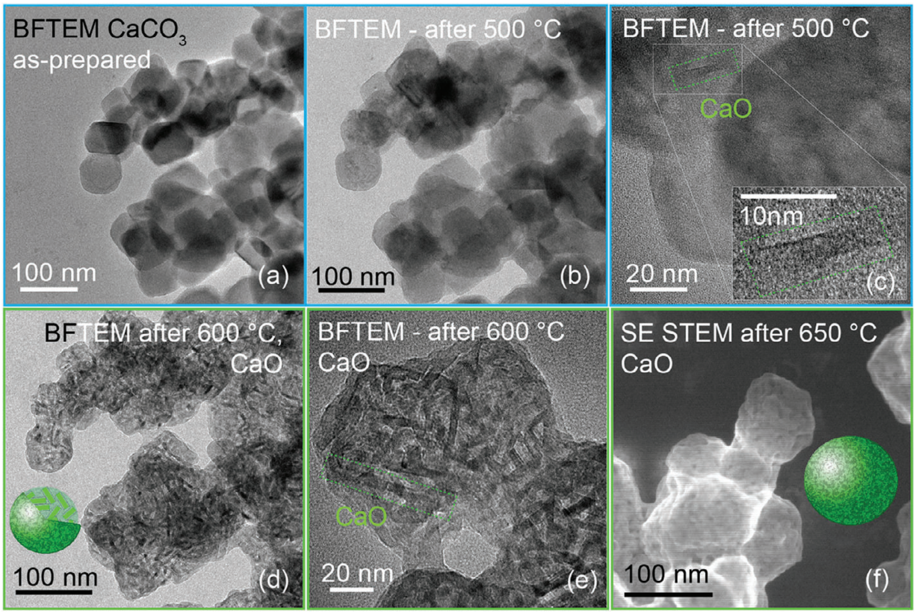

Figure 4. CaO crystallite and particle nanoporosity formation during calcination. a–c) The onset of calcination yielded isolated CaO crystallites 4 nm wide by 9 nm long after heating to 500 °C; crystallite size statistics are in Figure S9 (Supporting Information). d,e) CaO crystallite size after complete calcination increased to 5 nm by 22 nm after heating to 600 °C. f) In calcined CaO, correlated STEM SE and TEM BF imaging confirmed intraparticle nanoporosity is connected to the particle surface (Figure S10, Supporting Information). There was negligible particle coarsening during calcination, with the median particle size varying from 71 ± 3 nm to 69 ± 3 nm (Figure S12, Supporting Information).

elongation of the first CaO crystallite (green rectangle) confirms favorable CaO crystal growth under the reaction conditions. From 0.8–1.0 s, the reaction front consumes all remaining $CaCO_3$ and the converted CaO volume expands rightward. From 1.2–2.3 s, the reaction front propagates counterclockwise until the entire particle comprises CaO crystallites separated by nanoporosity (detailed later). The temporal evolution of the $CaCO_3$, reaction front, and CaO areas is visualized in Figure S9 (Supporting Information). After 20 s, the entire particle and surroundings are converted to nanoporous CaO, without additional particle shape or size change.

Beyond revealing a new calcination mechanism, in situ TEM imaging provided key practical detail about resultant nanoporous CaO particles, which is relevant in designing calcination-carbonation looping reactions. The onset of calcination (after 500 °C heating) formed rectangular rod-like CaO nanocrystals 4 nm wide and 9 nm long (outlined green in **Figure** 4a–c with statistics in Figure S10, Supporting Information). The lack of further CaO coarsening at 500 °C is attributed to the low temperature relative to the CaO Tammann temperature of > 1170 °C.[6,35] Further calcination (heating to 600 °C) yielded CaO nanocrystals 5 nm by 22 nm (Figure 4d,e; Figure S10, Supporting Information) with heating to 850 °C coarsening CaO to 33 nm by 51 nm (Figure S10, Supporting Information). The size of our CaO crystallites (4 nm by 9 nm at 500 °C, 5 nm by 22 nm at 600 °C, and 33 nm by 55 nm at 850 °C) is in agreement with the general trend observed in the literature that low-temperature decomposition yields the smallest stable CaO crystallites independent of CO_2 presence (27 nm at 800 °C and 76 nm at 1150 °C)[48] or metastable CaO (17 nm at 1000 °C and 47 nm at 1200 °C).[38] Correlated STEM SE imaging and TEM BF imaging elucidated the nanoporous nature of the CaO particles after calcination to unequivocally show that nanoscale porosity exists between CaO crystallites. Unlike TEM BF images which resolve CaO particle shape and crystallinity, the CaO particles' rough and dimpled surface can only be detected by surface-sensitive STEM SE imaging (Figure 4f). A direct comparison of TEM BF and STEM SE images from the exact same sample area confirmed that surface-connected nanoporosity separates CaO crystallites (Figure S11, Supporting Information). The CaO particle size statistical analysis of the images, which refers to the combined volume of the CaO rod-like crystallites and the intraparticle nanoporosity, recorded after heating to 500 °C and 600 °C revealed negligible particle coarsening during calcination, with the median particle size varying from 71 nm (as prepared) to 70 nm (after 500 °C) to 69 nm (after 600 °C), Figure S12 (Supporting Information).

3. Discussion

Our in situ calcination results are in contrast to the currently accepted shrinking core model [31,32] and grain model[52] (**Figure** 5a), which describe $CaCO_3$ calcination as a topotactic transformation initiated at the $CaCO_3$ surface and involving a reaction interface that travels radially inward toward the crystallite core with an intermediate metastable CaO by consuming unreacted $CaCO_3$ (Figure 5a i-ii) and leaves behind oriented CaO rod-like crystallites. Post-mortem SEM textural studies of calcination of millimeter size single crystals suggest calcination follows the shrinking core model because, at any point before reaction completion, an unreacted core of $CaCO_3$ surrounded by oriented CaO rod-like crystallites is observed.[41,48,53,54] The shrinking core (and grain) model assumes that $CaCO_3$ crystals

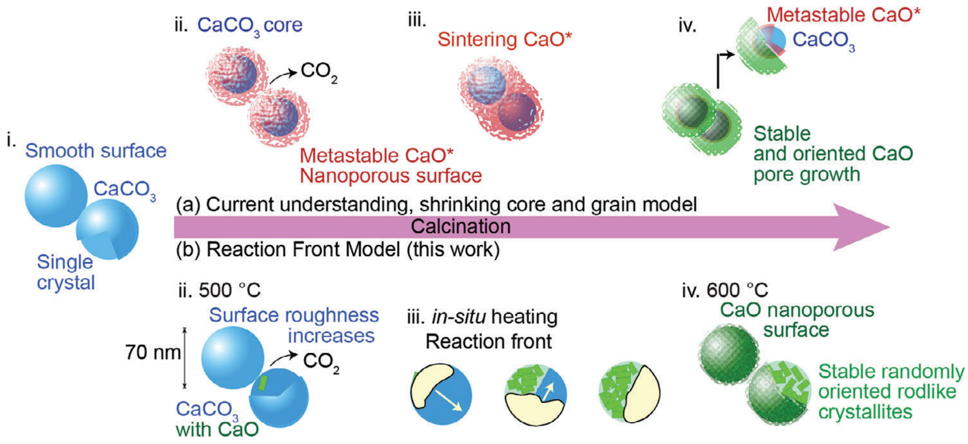

Figure 5. Calcite thermal decomposition mechanism according to a) the current understanding, shrinking core model, and grain model, compared to b) the reaction front model observed. (i) $CaCO_3$ single crystals in bulk and powder (a-ii) starting at the surface, chemical decomposition product is a metastable (strained rhombohedral[55] or cubic[38,40]) CaO form and CO_2 with the nanoporous surface. (a-iii) Strain accumulation leads to the aggregation of CaO[48] (a-iv) While the CO_2 desorbs the metastable structure collapses into stable CaO crystal with larger surface pores and the reaction region travels to the core. The result of calcination is a dual pore shell CaO structure with an unreactive calcite core, a metastable CaO intermediate that sinters before it is finally transformed into a stable CaO outer shell with a mesoporous surface. In contrast, (b-ii) at 500 °C we observe nucleation of stable CaO at preferred sites and higher particle surface roughness (c-iii) When heating to 600 °C, a reaction front nucleates at a grain boundary and travels perpendicular direction away leaving behind stable CaO nanocrystallites. As a result, particles with equivalent size and shape of the original calcite with a nanoporous surface made up of nano-size stable CaO crystallites.

decompose to an intermediate metastable polymorph of dilated cubic[38] or rhombohedral[55,56] CaO which forms a mesoporous surface layer comprising nanoscale metastable CaO crystallites whose thickness increases as the spherical reaction front proceeds inward and CO_2 gas diffuses outward. Because the Tammann temperature of stable CaO (1170–1310 °C) is substantially higher than typical calcination temperatures (>900 °C), sintering during calcination has been attributed to agglomeration and coarsening of the intermediate metastable CaO nanocrystallites due to exothermic stabilization to form the final stable CaO surface layer (Figure 5a-iii).[48,56] Before full calcination is reached, CaO agglomeration and sintering presumably limit the diffusion of CO_2 from core to surface[57] and limit the heat conduction into the reaction interface;,[58] both decrease the rate of the $CaCO_3$ decomposition close to equilibrium conditions (low-temperature) and become the rate-limiting factors (Figure 5a-iv). Compared to previous observations, the key role of particle-particle grain boundaries as heterogeneous nucleation sites and the reaction interface geometry (we show a planar cross-section that travels through the particle rather than a spherical surface moving toward the core) during nanoparticle calcination remained elusive due to the lack of time-resolved nanoscale resolution.

In contrast, our results indicate that nanoparticle calcination can involve planar reaction front motion following heterogenous CaO nucleation at $CaCO_3$ grain boundaries, without the formation of a metastable CaO polymorph intermediate (Figure 5b). At 500 °C, within a $CaCO_3$ particle, calcination proceeds first by increased particle surface roughness, attributed to calcination temperatures being in the range of the $CaCO_3$ Tammann temperature (533 °C)[34] which activates mass transport in $CaCO_3$ and heterogeneous nucleation of rectangular CaO crystals at $CaCO_3$ grain boundaries (Figure 5b i-ii). This is consistent with work showing that decreased calcite crystallinity increases the number of reactive sites near crystal defects, resulting in faster calcination.[51] Knowledge of the calcination onset and CaO nucleation temperatures is critical for designing solid-gas reactions in calcination/carbonation cycles where surface area loss at (energy-intensive) elevated temperatures causes rapid deactivation.[27,59] At 600 °C a dynamic reaction volume forms in which CaO crystallites nucleate with a planar reaction front that migrates laterally through the entire $CaCO_3$ particle in <3 s (Figure 5b-iii); rather than a spherical reaction front, as predicted by shrinking core and grain models, we observe a planar reaction front using in situ TEM and find no evidence for a metastable CaO reaction intermediate using in situ XRD.

Both our TEM observation and XRD analysis of nanoparticle calcination, in vacuum and inert gas conditions respectively, do not report metastable CaO. This finding agrees with the calcination studies conducted in vacuum of millimeter and micrometer size $CaCO_3$ particles.[37,48] In contrast, others have claimed the formation of a metastable (dilated) cubic CaO during decomposition under vacuum[38,54] and CO_2.[40,56] However, authors of seminal papers changed their interpretation and no longer claimed the existence of an intermediate state.[41] Recent experimental evidence of decomposition in the presence of CO_2[40] could be alternatively interpreted as showing that the metastable CaO has a crystal structure closer to the rhombohedral $CaCO_3$ than cubic CaO.[55] Calcination studies in the presence of $\geq 60\%$ CO_2, Valverde et al. reported a new metastable CaO with peaks (111) and (311) overlapping with the carbonate hexagonal rhombohedral peaks (104) and (122).[40] That work, using XRD, showed that the unit cell contraction between metastable and stable CaO was found to be 8%, with the metastable phase requiring ≈60 min to disappear during calcination under 60% CO_2 at 900 °C. While it is impossible to deny that there might exist a metastable CaO that appears and disappears within 5 min, we can assert that within the confines of this study, we did not observe any potential metastable phase. Compared only to the calcination studies in vacuum or inert conditions we agree with the early and recent work,[37,48] including the seminal work whose data interpretation changed and asserts there is no metastable CaO intermediate in the calcination of $CaCO_3$ in the absence of CO_2.[41]

When the $CaCO_3$ particle fully decomposes, a nanoporous CaO particle remains that is equal in dimension, with surface-connected nanopores between stable and randomly oriented rodlike CaO crystals (Figure 5b-iv). Previous studies have shown millimeter-size $CaCO_3$ calcination by topotactic decomposition with a preferred crystallographic orientation between $CaCO_3$ and CaO product, resulting in oriented CaO rodlike crystallites.[48,53,54,60] Instead, we observe randomly spatially oriented CaO crystallites (Figure 4e), which we hypothesize are a result of CO_2 diffusion lengths (≈35 nm, or half of the 70-nm particle size used here) shorter than the critical diffusion length of CO_2 through $CaCO_3$ known to kinetically limit CO_3^{2-} egress (49–90 nm[61,62]). We have no evidence that our calcined CaO crystallites are preferentially topotactic toward $CaCO_3$. Sufficiently short diffusion lengths could potentially allow isotropic CO_2 release (more specifically CO_3^{2-}) from nanoparticles, as opposed to anisotropic CO_2 release characteristic in much larger particles. This also agrees with Singh et al.'s study of $CaCO_3$ (sized 200 nm by ≈1 µm) calcination that resulted in misoriented CaO rodlike crystallites.[63] The different observations support that nanoparticle calcination results in a misoriented CaO product in contrast to oriented CaO in larger $CaCO_3$ particle calcination.

Absent evidence for metastable CaO—whose exothermic stabilization is often cited as the driving force for CaO aggregation and sintering, we hypothesize that the tendency of CaO nanoparticles to spontaneously lower surface-area-to-volume ratio is driven by surface energy minimization. Importantly for future applications, the nanoporous CaO microstructure produced by calcination is expected to enhance reactivity with CO_2, as decreasing CaO crystallite size has been linked to maximized carbonation conversion over repeated cycles[64] and more efficient CO_2 capture and looping technologies.[65] Necessary to be suitable for carbon sequestration or utilization, high-purity high-concentration CO_2 streams are desired, which result from calcination in a CO_2 and/or steam-rich environment that affects both the rate and extent of sintering. Based on our results, we hypothesize that because calcination of nanoscale $CaCO_3$ at 500–600 °C yields the minimum CaO crystallite size and high-surface-area surface-connected nanoporosity, this calcination condition could be used to both inhibit sorbent deactivation via particle coarsening and facilitate rapid subsequent carbonation in applications where calcination can be performed under low CO_2 partial pressures, such as calcium looping methane reforming.[66,67]

In summary, we uncovered a new $CaCO_3$ calcination mechanism involving heterogeneous nucleation of nanoporous CaO at $CaCO_3$ grain boundaries followed by planar reaction front motion, in contrast to the widely accepted spherical shrinking core model. Using nanoscale time-resolved observations of the thermal decomposition of $CaCO_3$, we show that CaO crystallite formation is complete after 2.5 s at 600 °C. Furthermore, using synchrotron X-ray diffraction we did not observe the controversial metastable strained CaO, instead $CaCO_3$ converted directly to the thermodynamically stable form of CaO whose lattice constant agrees with that calculated by density functional theory. Formation of CaO crystallites into nanoporous particles occurs at distinctly lower temperatures than surface area loss via particle sintering at higher temperatures. This is important technologically in applications where CO_2 pressures can be depressed intentionally, such as looping reforming. Moreover, the correct conceptual model allows for the design of new and possibly more favorable operating conditions for calcination and predicts the behavior of similar reactions. Additionally, this nanoporous morphology offers a higher surface-area-to-volume ratio, expected to be more reactive with CO_2 during carbonation.

4. Experimental Section

Sample Preparation for In Situ (Scanning) Transmission Electron Microscopy ((S)TEM): 20 nm $CaCO_3$ particles of 99.9% purity and coated in stearic acid to prevent spontaneous particle coarsening (R-3c, hexagonal Calcite, GetNanoMaterials, Las Cruces, USA) were diluted with isopropanol into a 0.01 g mL^{-1} white homogenous solution. The solution was sonicated for 1 h at 65 °C where the particles coarsened to 70 nm. A droplet of solution was deposited on a free-standing electron transparent amorphous silicon nitride film embedded on a MEMS heating chip (Fusion, Protochips, Morrisville, USA). To ensure this procedure did not alter the particles' crystal structure, the same sample preparation was used to yield several grams of powder for ex situ XRD characterization (Cu K_α radiation). The above steps were repeated, and the isopropanol evaporated at ambient temperature and environment overnight. The resulting dried powder was deposited on a single crystal Si wafer with silicon nitride coating to replicate the MEMS heating chip substrate.

(S)TEM Characterization: All (S)TEM experiments used a 200 kV (S)TEM (JEM-2800, JEOL Ltd., Akishima, Japan). The electron beam tuning was limited to areas of the electron transparent chip windows which were excluded from experimental data collection. TEM SAED patterns were collected in the same regions which were avoided for (S)TEM imaging. To determine the calcination onset temperatures and products, a first in situ experiment heated the sample stepwise to temperatures between 300 and 900 °C at 1200 °C s^{-1} with nearly instantaneous cooling to room temperature in between. In a second experiment, a sample was similarly heated to 500, 600, and 650 °C. TEM SAED patterns and (S)TEM images were collected at 25 °C between heating steps; in situ TEM bright field video was collected during heating at 600 °C.

In Situ Synchrotron X-Ray Diffraction (XRD) by Wide Angle X-Ray Scattering: The synchrotron XRD diffraction of 90 nm $CaCO_3$ (R-3c, hexagonal Calcite, PlasmaChem GmbH, Adlershof, Germany) of 99.9% purity was performed at the beamline 9-ID-C in the Advanced Photon Source, at the Argonne National Laboratory, Lemont, IL, USA, using the ultra-small-angle X-ray scattering beamline.[68] The $CaCO_3$ particles were packed into a quartz capillary of 0.9-mm inner diameter, with particles immobilized by glass wool at either end. The particles were heated with resistive coils placed on the top and bottom, with a K-type thermocouple inside the capillary to continuously monitor and control the temperature/current. A continuous flow of N_2 gas was passed through the capillary, and monitored by a bubbler for continuous flow during the experiment. The sample was heated to 40 °C, then 500 °C, and finally to 600 °C and held for 8, 100, and 52 min, respectively, at each temperature. The analysis was conducted at the National Institute of Standards and Technology. Diffraction peaks were fitted using the Voigt fit function implemented with OriginLab NLFit interface (version 2023, OriginLab, Northampton, USA).

Density Functional Theory (DFT) Calculations: Spin-polarized DFT[69,70] calculations were performed using the generalized gradient approximation (GGA) with the Perdew–Burke–Ernzerhof (PBE)[71] exchange-correlation function. Within the GGA formalism, Kohn–Sham equations were solved using the plane wave basis and used with the projected augmented wave (PAW),[72] method as implemented in the Vienna ab initio Simulation Package (VASP).[73,74] A plane-wave cutoff energy of 400 eV was utilized to ensure accurate results, which converged the total energies to ≈0.01 meV. The irreducible Brillouin-zone integrations were performed using Monkhorst–Pack grid[75] of 10 × 10 × 10 with Gaussian smearing of 0.1 eV. CaO in cubic rocksalt phase was modeled using a $2 \times 2 \times 2$ supercell comprising 64 atoms, 32 of each species. Geometry optimization was achieved by minimizing the Hellman–Feynman forces until the total forces on each atom were <0.01 eV Å^{-1}. DFT calculations were performed using the Extreme Science and Engineering Discovery Environment (XSEDE) resources.[76]

Statistical Analysis: Figure 2c, As described in the figure caption, uncertainty bars indicate the estimated precision of the measured peak position of ± 1 channel in the synchrotron XRD pattern. (Figure S5, Table S2, Supporting Information) Using the CaO (220) XRD peak fitted to the Voigt function the CaO lattice constant is calculated to be 4.841 Å ± 0.007 Å at 600 °C. The CaO lattice constant, corrected for thermal expansion is calculated to be 4.805 Å ± 0.007 Å. The average r-squared of the Voigt fitting is 0.9954. (Figure S6, Supporting Information) Time-resolved XRD patterns were fitted to the Voigt function. The shaded regions indicate uncertainty of the fit in the (a-b) full-width half maxima (FWHM) and the (c-d) area of the XRD peaks. (Figure S10, Supporting Information) CaO crystallite size measured from BFTEM images is 4 nm by 9 nm at 500 °C, 5 nm by 22 nm at 600 °C, and 33 nm by 55 nm at 850 °C. The shaded red and black regions indicate one standard deviation; dotted lines show the linear fit. (Figure S12, Supporting Information) Statistical analysis of particle diameter represented by the area delineated in $CaCO_3$ (blue) and CaO (green) before and after calcination, measured from BFTEM images. The median particle size and size distribution vary negligibly, from 71 ± 3 nm to 69 ± 3 nm. Each particle perimeter was manually outlined, and Matlab code was used to measure 180 diameters for each particle at every 1° of diameter rotation. Red lines/numbers indicate the standard deviation. The sample size *n* before calcination (25 °C), after heating to 500 °C and 600 °C is 229, 155, and 137 particles respectively.

Supporting Information

Supporting Information is available from the Wiley Online Library or from the author.

Acknowledgements

J.M. and W.J.B. acknowledge support from the National Science Foundation Graduate Research Fellowship Program (NSF GRFP) and the Climate Pathfinders Foundation. J.W. and W.J.B. acknowledge support from the NSF CAREER (DMR-2042638). H.G. and W.J.B. acknowledge support from the American Chemical Society's Petroleum Research Fund (ACS PRF Grant PRF# 61961-DNI). The authors acknowledge the use of facilities and instrumentation at the UC Irvine Materials Research Institute (IMRI), which was supported in part by the National Science Foundation through the UC Irvine Materials Research Science and Engineering Center (MRSEC DMR-2011967). P.P.D. and J.R. acknowledge support from the NSF CAREER (DMR-2042311). This work used an Extreme Science and Engineering Discovery Environment (XSEDE), which was supported by NSF grant number ACI-1548562. L.D-M., L.M., and X.Z. acknowledge support from the Precourt Center for supporting their contributions to the work. This research used resources of the Advanced Photon Source, a U.S. Department of Energy (DOE) Office of Science user facility operated for the DOE Office of Science by Argonne National Laboratory under Contract No. DE-AC02-06CH11357.

Conflict of Interest

The authors declare no conflict of interest.

Author Contributions

W.J.B., J.M., and J.W. conceived the study and designed the (S)TEM experiment. J.M. prepared the samples. J.W. and J.M. performed the (S)TEM experiments. J.M. and J.M. analyzed (S)TEM data. X.Z., L.M., I.K., J.I., F.Z, and L. D-M collected the synchrotron XRD data. H.G. conducted the XRD. J.R. conducted DFT calculations under the supervision of P.P.D., J.M., and W.J.B. wrote the manuscript and all the authors contributed to its revision. W.J.B. supervised the project.

Data Availability Statement

The data that support the findings of this study are available in the supplementary material of this article.

Keywords

$CaCO_3$, calcination, in situ synchrotron X-ray diffraction, in situ transmission electron microscopy, nanoparticle, nanoporosity, sintering

Received: September 26, 2023
Revised: March 20, 2024
Published online: April 5, 2024

[1] C. Y. Tai, F.-B. Chen, *AIChE J.* **1998**, *44*, 1790.
[2] J. D. O'Keefe, T. J. Ahrens, *Nature* **1989**, *338*, 247.
[3] J. W. Morse, G. M. Marion, *Am. J. Sci.* **1999**, *299*, 738.
[4] A. J. Carrillo, J. González-Aguilar, M. Romero, J. M. Coronado, *Chem. Rev.* **2019**, *119*, 4777.
[5] C. Ortiz, J. M. Valverde, R. Chacartegui, L. A. Perez-Maqueda, P. Giménez, *Renew Sustain. Energy Rev.* **2019**, *113*, 109252.
[6] R. Han, Y. Wang, S. Xing, C. Pang, Y. Hao, C. Song, Q. Liu, *Chem. Eng. J.* **2022**, *450*, 137952.
[7] D. W. Keith, G. Holmes, D. S. Angelo, K. Heidel, *Joule* **2018**, *2*, 1573.
[8] N. McQueen, P. Kelemen, G. Dipple, P. Renforth, J. Wilcox, *Nat. Commun.* **2020**, *11*, 3299.
[9] M. Erans, S. A. Nabavi, V. Manović, *Energy Convers. Manag. X* **2019**, *1*, 100007.
[10] X. Zhang, H. Geng, X. Zhang, Y. Liu, J. Hao, J. Cui, *J. Mater. Chem. A* **2023**, *11*, 2996.
[11] A. Kätelhön, R. Meys, S. Deutz, S. Suh, A. Bardow, *Proc. Natl. Acad. Sci.* **2019**, *116*, 11187.
[12] C. Hepburn, E. Adlen, J. Beddington, E. A. Carter, S. Fuss, N. Mac Dowell, J. C. Minx, P. Smith, C. K. Williams, *Nature* **2019**, *575*, 87.
[13] A. Imhof, *Renew. Energy* **1997**, *10*, 239.
[14] D. P. Hanak, M. Erans, S. A. Nabavi, M. Jeremias, L. M. Romeo, V. Manovic, *Chem. Eng. J.* **2018**, *335*, 763.
[15] E. D. Lena, M. Spinelli, M. C. Romano, *Energy Procedia* **2018**, *148*, 186.
[16] L. M. Mukhin, A. P. Koscheevi, Y. P. Dikov, J. Huth, H. Wänke, *Nature* **1996**, *379*, 141.
[17] B. Sweeney, RECAST – A System to Decarbonise Long-distance Shipping, **2020**, https://calix.global/wp-content/uploads/2020/09/INEC2020-RECAST-a-system-to-decarbonise-shipping-V04c.pdf.
[18] G. Ounoughene, E. Buskens, R. M. Santos, Ö. Cizer, T. Van Gerven, *J. CO2 Util.* **2018**, *26*, 143.
[19] J. Wang, R. Fu, S. Wen, P. Ning, M. H. Helal, M. A. Salem, B. B. Xu, Z. M. El-Bahy, M. Huang, Z. Guo, L. Huang, Q. Wang, *Adv. Compos. Hybrid Mater.* **2022**, *5*, 2721.
[20] K. Kyaw, H. Matsuda, M. Hasatani, *J. Chem. Eng. Jpn.* **1996**, *29*, 119.
[21] F. Raganati, P. Ammendola, *Energy Fuels* **2023**, *37*, 1777.
[22] A. K. Galwey, M. E. Brown, *J. Therm. Anal. Calorim.* **2000**, *60*, 863.
[23] B. V. L'vov, L. K. Polzik, V. L. Ugolkov, *Thermochim. Acta* **2002**, *390*, 5.
[24] A. K. Galwey, M. E. Brown, *Thermochim. Acta* **2002**, *386*, 91.
[25] M. Krödel, A. Landuyt, P. M. Abdala, C. R. Müller, *ChemSusChem* **2020**, *13*, 6259.

[26] L. Fedunik-Hofman, A. Bayon, S. W. Donne, *Energies* **2019**, *12*, 2981.
[27] G. S. Grasa, J. C. Abanades, *Ind. Eng. Chem. Res.* **2006**, *45*, 8846.
[28] Y. Zhu, S. Wu, X. Wang, *Chem. Eng. J.* **2011**, *175*, 512.
[29] A. A. Matvienko, S. A. Chizhik, A. A. Sidel'nikov, *Dokl. Phys. Chem.* **2013**, *451*, 184.
[30] P. Sun, J. R. Grace, C. J. Lim, E. J. Anthony, *AIChE J.* **2007**, *53*, 2432.
[31] V. Golubev, D. Chistyakov, D. Mayorov, E. Fomichev, I. Blednykh, in *Light Metals 2022*, (Ed.: D. Eskin), Springer International Publishing, Cham, **2022**, pp. 11–21.
[32] M. Broda, R. Pacciani, C. R. Müller, in *Porous Materials for Carbon Dioxide Capture* (Eds. A.-H. Lu, S. Dai), Springer, Berlin, Heidelberg, **2014**, pp. 181–222.
[33] J. Manuel Valverde, *J. Mater. Chem. A* **2013**, *1*, 447.
[34] W. Yue, C. Fan, W. Song, S. Li, *J. Environ. Chem. Eng.* **2022**, *10*, 107440.
[35] H. Lu, A. Khan, S. E. Pratsinis, P. G. Smirniotis, *Energy Fuels* **2009**, *23*, 1093.
[36] D. Beruto, A. W. Searcy, *Nature* **1976**, *263*, 221.
[37] K. M. Towe, *Nature* **1978**, *274*, 239.
[38] S. Dash, M. Kamruddin, P. K. Ajikumar, A. K. Tyagi, B. Raj, *Thermochim. Acta* **2000**, *363*, 129.
[39] J. M. Valverde, *Chem. Eng. Sci.* **2015**, *132*, 169.
[40] J. M. Valverde, S. Medina, *Phys. Chem. Chem. Phys.* **2015**, *17*, 21912.
[41] E. K. Powell, A. W. Searcy, *J. Am. Ceram. Soc.* **1982**, *65*, C42.
[42] B. R. Stanmore, P. Gilot, *Fuel Process. Technol.* **2005**, *86*, 1707.
[43] Z. Li, X. Guo, X. Xue, X. Xu, B. Wang, *Ind. Eng. Chem. Res.* **2023**, *62*, 4851.
[44] H. Vahidi, K. Syed, H. Guo, X. Wang, J. L. Wardini, J. Martinez, W. J. Bowman, *Crystals* **2021**, *11*, 878.
[45] J. L. Wardini, H. Vahidi, H. Guo, W. J. Bowman, *Front Chem* **2021**, *9*.
[46] N. H. Florin, A. T. Harris, *Chem. Eng. Sci.* **2009**, *64*, 187.
[47] S. F. Wu, Q. H. Li, J. N. Kim, K. B. Yi, *Ind. Eng. Chem. Res.* **2008**, *47*, 180.
[48] C. Rodriguez-Navarro, E. Ruiz-Agudo, A. Luque, A. B. Rodriguez-Navarro, M. Ortega-Huertas, *Am. Mineral.* **2009**, *94*, 578.
[49] R. Srinivasan, *Proc. Indian Acad. Sci. – Sect. A* **1955**, *42*, 81.
[50] R. Ruppin, *Solid State Commun.* **1972**, *10*, 1053.
[51] J. M. Valverde, P. E. Sanchez-Jimenez, L. A. Perez-Maqueda, *Environ. Sci. Technol.* **2014**, *48*, 9882.
[52] Z. Li, *Chem. Eng. Sci.* **2020**, *227*, 115902.
[53] D. M. Fenwick, *Part 1: The Effect of Lattice Defects on the Sintering of Lithium Fluoride; Part 2: The Morphology of Calcium Oxide from Calcium Carbonate Decomposition*. Lawrence Berkeley National Laboratory eScholarship, **2020**, p. 64.
[54] D. Beruto, A. W. Searcy, *J. Chem. Soc. Faraday Trans. 1 Phys. Chem. Condens. Phases* **1974**, *70*, 2145.
[55] E. P. Hyatt, I. B. Cutler, M. E. Wadsworth, *J. Am. Ceram. Soc.* **1958**, *41*, 70.
[56] J. M. Valverde, P. E. Sanchez-Jimenez, L. A. Perez-Maqueda, *J. Phys. Chem. C* **2015**, *119*, 1623.
[57] R. H. Borgwardt, *AIChE J.* **1985**, *31*, 103.
[58] A. W. D. Hills, *Chem. Eng. Sci.* **1968**, *23*, 297.
[59] J. M. Valverde, *Chem. Eng. J.* **2013**, *228*, 1195.
[60] D. Beruto, L. Barco, A. W. Searcy, *J. Am. Ceram. Soc.* **1983**, *66*, 893.
[61] D. Alvarez, J. C. Abanades, *Ind. Eng. Chem. Res.* **2005**, *44*, 5608.
[62] H. Sun, J. Wang, X. Liu, B. Shen, C. M. A. Parlett, G. O. Adwek, E. John Anthony, P. T. Williams, C. Wu, *J. Mater. Chem. A* **2019**, *7*, 9977.
[63] A. Singh, S. Dash, M. Kamruddin, P. K. Ajikumar, A. K. Tyagi, V. S. Raghunathan, B. Raj, *J. Am. Ceram. Soc.* **2004**, *85*, 927.
[64] A. Biasin, C. U. Segre, G. Salviulo, F. Zorzi, M. Strumendo, *Chem. Eng. Sci.* **2015**, *127*, 13.
[65] G. Sneddon, A. Greenaway, H. H. P. Yiu, *Adv. Energy Mater.* **2014**, *4*, 1301873.
[66] S. Jo, J. H. Woo, T. Nguyen, J. E. Kim, T. Y. Kim, H.-J. Ryu, B. Hwang, J. C. Kim, S. C. Lee, K. L. Gilliard-AbdulAziz, *Energy Fuels* **2023**, *37*, 19680.
[67] S. Tian, F. Yan, Z. Zhang, J. Jiang, *Sci. Adv.* **2019**, *5*, eaav5077.
[68] J. Ilavsky, F. Zhang, R. N. Andrews, I. Kuzmenko, P. R. Jemian, L. E. Levine, A. J. Allen, *J. Appl. Crystallogr.* **2018**, *51*, 867.
[69] P. Hohenberg, W. Kohn, *Phys. Rev.* **1964**, *136*, B864.
[70] W. Kohn, L. J. Sham, *Phys. Rev.* **1965**, *140*, A1133.
[71] J. P. Perdew, K. Burke, M. Ernzerhof, *Phys. Rev. Lett.* **1996**, *77*, 3865.
[72] P. E. Blöchl, *Phys. Rev. B* **1994**, *50*, 17953.
[73] G. Kresse, J. Hafner, *Phys. Rev. B* **1993**, *47*, 558.
[74] G. Kresse, J. Furthmüller, *Phys. Rev. B* **1996**, *54*, 11169.
[75] H. J. Monkhorst, J. D. Pack, *Phys. Rev. B* **1976**, *13*, 5188.
[76] J. Towns, T. Cockerill, M. Dahan, I. Foster, K. Gaither, A. Grimshaw, V. Hazlewood, S. Lathrop, D. Lifka, G. D. Peterson, R. Roskies, *Comput. Sci. Eng.* **2014**, *16*, 62.